One-step solid-state synthesis of NixPy@C nanocomposites for high-performance hybrid supercapacitor

Shiyao Gao[1], Bing Wang[1], Deyi Zhang[1], Xu Xia[1], Jingruo Wang[1], Wenna She[1], Biao Yang[1], Xianxin Meng[1], Kunjie Wang[1], and Zhiyong Han[1]

[1]Lanzhou University of Technology

May 16, 2022

Abstract

In this work, a convenient and efficient one-step solid-phase synthesis method (SPS) is successfully developed for the preparation of NixPy@C nanocomposites under an ambient atmosphere. By controlling the synthesizing temperature, carbon-coated Ni2P, Ni5P4, and NiP2 nanocomposites can be facilely synthesized. The solid-phase synthesized NixPy@C nanocomposites exhibit high charge storage capability and good cycle stability. A high specific capacity of over 197.2 mAh g-1 (709.9 C g-1) is achieved at a current density of 1 A g-1 for the optimal nanocomposite NiP2@C. The assembled hybrid supercapacitor device based on the NiP2@C nanocomposite and an interconnected hierarchical porous carbon (NiP2@C//IHPC) delivers a specific energy of up to 50.38 Wh kg-1 at a specific power of 0.89 kW kg-1. More than 83.8% of initial specific capacity is retained after 20000 cycles. This method is proved to be a reliable strategy for simple preparation of high-performance transition metal phosphides for energy storage devices.

1. Introduction

In recent years, with the rapid development of new energy vehicles and portable electronic equipment, more and more attention has been attracted to the electrochemical energy storage devices represented by various batteries and supercapacitors (SCs) [1,2]. Ascribed to the distinguished power density, cycle life, and safety, supercapacitors are considered promising next-generation energy storage devices [1-3]. According to different energy storage mechanisms, supercapacitors can be categorized into electric double-layer capacitors (EDLCs), pseudocapacitors (PSCs), and hybrid supercapacitors (HSCs) [3]. EDLCs generally use carbon materials with large specific surface areas and tailorable morphologies, such as graphene, porous carbon, and carbon nanotubes, as electrode materials [2,4,5]. Unfortunately, the physical energy storage mechanism induces low charge storage capability for carbon materials and unsatisfactory energy density for EDLCs[5]. The deficiencies of PSCs are their low power density and inferior cycle durability caused by poor conductivity and bad structural stability of pseudocapacitive electrode materials, such as transition metal oxides/sulfides/phosphide or conducting polymers[6,7]. Meanwhile, EDLCs and PSCs generally exhibit low operating voltage ([?]1 V), which also obstructs achieving high energy density. By using carbon materials as the negative electrode and battery-like pseudocapacitive materials as the positive electrode, hybrid supercapacitors can be constructed to harvest high energy density without sacrificing high power density and long cycle durability by effectively utilizing the different potential windows between the two kinds of electrodes to widening operating voltage (>1.5 V) and combining the characteristic of EDLCs and PSCs [8]. Thus, hybrid supercapacitors are considered as promising next-generation supercapacitors[9,10].

Ascribed to the high theoretical specific capacity generated by the reversible redox reaction rapidly occurring at the interface between the electrode and electrolyte, transition metal oxides (TMOs), such as NiO[11], MnO_2 [12], and V_2O_5 [13], have been used as electrode materials of PSCs or HSCs. However, the poor electrical conductivity and bad structural stability of TMOs are not conducive to the fast electron transport required

by high power density and thus obstruct their practical application in supercapacitors[14,15]. Alternatively, transition metal phosphides (TMPs) exhibit larger theoretical capacitance and higher conductivity than TMOs, which can be used as promising battery-like materials for HSCs and LiBs [16-18]. In addition, TMPs also show excellent physical and chemical properties, such as better structural stability and corrosion resistance in typical acid and alkali environments [17]. Therefore, TMPs, such as Ni_xP_y [19-21], CoP[22,23], Cu_3P [24], and multicomponent TMPs [25-28], have recently been considered as candidates to replace traditional TMOs as the high-performance electrode materials for energy storage applications. Among them, various nickel phosphides (Ni_xP_y) attracted the most attention due to their high-performance exhibited in practical application. For instance, the honeycomb-like biphasic Ni_5P_4–Ni_2P nanosheets reported by Liu et al. delivered a high specific capacity of 1272 C g^{-1} at a current density of 2 A $g^{-1}$with high rate capability (over 64% capacity retention at 10 A g^{-1}) and good cycle stability (90.9% capacity retention after 5000 cycles) [21], while the $Ni_{12}P_5$ nanowires with high conductivity prepared by Gan et al. displayed a reversible specific capacity of 707.2 C g^{-1} at 1 A g^{-1} and good cyclic stability, over 68% of capacity was retained at 10 A g^{-1} [20].

The preparation of TMPs is very challenging. Generally, the phosphating process is complicated and has limited controllability. Presently, the two-step (post phosphating) method is the dominant strategy to obtain TMPs. In this method, transition metal hydroxide/sulfide or MOF is prepared as a precursor by the hydrothermal (liquid-phase synthesize) method, and then the phosphating is performed by treating the precursor with methylene phosphorus in an inert atmosphere under high temperature [16,18,29]. This synthesis process is cumbersome and time-consuming while producing harmful wastewaters and toxic PH_3 gas, making it less cost-effective and eco-friendly. The solid-phase synthesis (SPS) method can avoid the use of solvents and surfactants, thus making the preparation process easy, efficient, cost-efficiency, and eco-friendly[24,30]. In our previous works, we successfully developed a facile SPS method for controllably preparing transition metal sulfides and their nanocomposites [30,31]. The prepared layered NiS/rGO nanocomposite exhibits an ultrahigh specific capacity of 299.7 mAh g^{-1} at a current density of 2 A $g^{-1}$and good capacity retention at 15 A g^{-1} (161.2 mAh g^{-1}) [30], proving the feasibility and advantage of the SPS method for synthesizing transition metal sulfides. The SPS method also is expected to be a promising strategy for preparing TMPs. To the best of our knowledge, preparing TMPs by a one-step SPS method is rarely reported.

In this work, we developed a convenient and efficient one-step SPS method for the target-oriented synthesis of carbon-coated Ni_2P, Ni_5P_4, and NiP_2 nanocomposites (Ni_xP_y@C). By one-step calcining the solid-phase mixture of nickel formate and triphenylphosphine (PPH3) powder in a sealed stainless steel autoclave and adjusting the synthesizing temperature, Ni_2P@C, Ni_5P_4@C, or NiP_2@C nanocomposite can be facilely synthesized. The carbon-coated structure is conducive to accelerating the reaction kinetics and relieving the volumetric expansion of Ni_xP_ynanoparticles during the charging/discharging process[19,32]. The solid-phase synthesized Ni_xP_y@C nanocomposites exhibit high charge storage capability and good cycle stability. A high specific capacity of over 197.2 mAh g^{-1} (709.9 C g^{-1}) is achieved at a current density of 1 A g^{-1} for the optimal nanocomposite NiP_2@C, and more than 84.3% of initial specific capacitance is kept after 1000 cycles. The HSC (NiP_2@C//IHPC) device was assembled by using the prepared NiP_2@C nanocomposites as the positive electrode material and the interconnected hierarchical porous carbon (IHPC) reported in our previous work as the negative electrode material[33], and exhibits a specific capacity of up to 63.0 mAh g^{-1} at a current density of 1 A $g^{-1}$and good cycle retention of over 83.8% after 20000 cycles. A specific energy of up to 50.38 Wh kg^{-1} is delivered at a specific power of 0.89 kW kg^{-1} for the assembled NiP_2@C//IHPC device, which value still reaches 29.1 Wh kg^{-1} at a high specific power of 9.44 kW kg^{-1}. More than 83.8% of initial specific capacity is retained after 20000 cycles. The successfully developed solid-phase synthesis method is proved to be a reliable strategy for facile preparation of TMPs with high performance.

2. Experimental section

2.1 Synthesis of Ni_xP_y@C nanocomposites

Ni_xP_y@C nanocomposites are easily synthesized through a facile and efficient one-step SPS route. In the details, 0.15 g of nickel formate and 1.313 g of PPH3 powder were mixed and ground to form a uniform solid-phase mixture under the ambient atmosphere. The molar ratio of Ni and P in the initial mixture was

1:5. The mixture was sealed in a 25 ml stainless steel autoclave with a stainless steel inner tank, and then calcined at the temperature of 300˜450°C for 2 hours under an ambient atmosphere. After cooling to ambient temperature, the powder dispersed in the oil phase was stirred and washed with CCl_4, and then rinsed with alcohol. Finally, the washed sample was vacuum dried to obtain Ni_xP_y@C nanocomposites.

3. Results and discussion

Ni_xP_y@C nanocomposites are one-step synthesized by directly calcining the mixture of nickel formate and PPH3 powder in a stainless steel autoclave under an ambient atmosphere. As shown in Fig. 1, PPh3 melts into the liquid phase and uniformly coats the surface of nickel formate powder when the synthesizing temperature is high than the melting point of PPH3 (78.5 81.5degC). Then, nickel formate powders decomposite into Ni nanoparticles when the synthesizing temperature is higher than 210degC [34]. The fresh Ni nanoparticles are coated by PPh3 quickly and further react with PPh3 to form complex tetrakis(triphenylphosphine)nickel(0) ($Ni[PPh3]_4$) [35]. As the synthesizing temperature continually rises to higher than 300degC, the complex $Ni[PPh3]_4$ decomposites into NiP_2, Ni_5P_4, or NiP_2 nanoparticles (depending on the synthesizing temperature) and polycyclic aromatic hydrocarbons (PAHs). The Ni_xP_y nanoparticles are coated by the PAHs, which avoids the agglomeration of Ni_xP_y nanoparticles. As well as known, Ni_xP_y is an excellent dehydrogenation catalyst [36,37]. Ascribing to the catalytic effect of Ni_xP_y along with the high temperature and high pressure in the sealed autoclave, some of the PAHs coated on the surface of Ni_xP_ynanoparticles are further converted into carbon to coated on the surface of Ni_xP_y nanoparticles to form Ni_xP_y@C nanocomposites.

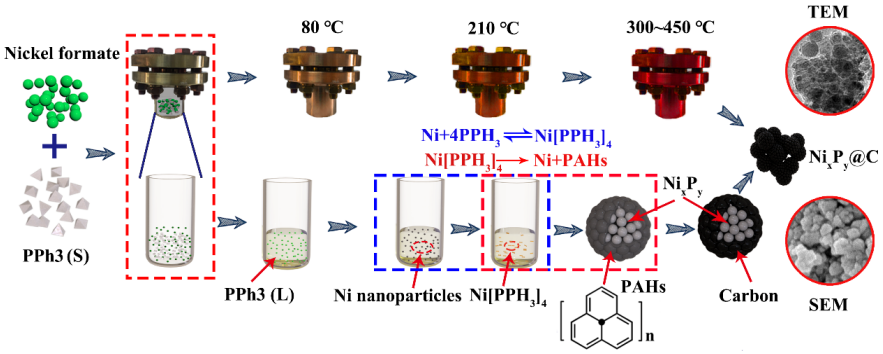

Fig. 1 the scheme for the solid-phase synthesis of Ni_xP_y@C nanocomposites

The phase composition of Ni_xP_ynanoparticles in the nanocomposites can be controlled by adjusting the synthesizing temperature between 300˜400°C. As shown in Fig. 2a, the XRD spectrum of the sample prepared at 300°C exhibits strong diffraction peaks at 2ϑ angles of 40.7°, 44.6°, 47.4°, 54.2°, and 74.8°, corresponding to the (111), (201), (210), (300), and (400) crystal planes of hexagonal Ni_2P [38]. For the sample fabricated at 350°C, the strong diffraction peaks at 30.4°, 40.6°, 47.0°, 52.9°, and 53.9° refer to the (200), (210), (301), (214), and (220) crystal planes of hexagonal Ni_5P_4 (Fig. 2b) [39]. Under the synthesizing temperature of 400°C, monoclinic NiP_2 is successfully synthesized. As shown in Fig. 2c, the narrow diffraction peaks at 28.2°, 32.7°, 36.7°, 40.3°, 46.9°, 55.6°, and 63.6° correspond to the (111), (200), (210), (211), (220), (311), and (321) crystal plane of monoclinic NiP_2[40]. It can be seen that NiP_2, Ni_5P_4, and NiP_2 can be directionally synthesized by controlling the synthesizing temperature at 300, 350, and 400°C, respectively. The adjusting function of synthesizing temperature on the phase composition of Ni_xP_y nanoparticles loses efficacy as the temperature is higher than 400°C. As shown in Fig. 2c, the sample obtained at 450°C displays the same phase as the sample prepared at 400°C. Meanwhile, the synthesizing temperature exhibits an apparent effect on the crystallinity and crystallite dimension of the obtained Ni_xP_y nanocomposites. With the increasing synthesizing temperature, the diffraction peaks of the Ni_xP_y nanocomposites become narrow and strong, illuminating the improvement of the crystallinity and crystallite dimension. Besides the strong and narrow diffraction peaks of Ni_xP_y, an apparent hump peak centered at ca 26°is observed for all nanocomposites, indicating the existence of amorphous carbon and successful synthesis of Ni_xP_y@C nanocomposites[41].

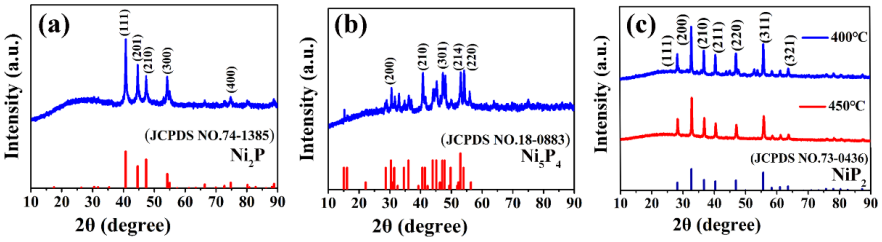

Fig. 2 XRD spectra of the prepared NiP_2@C (a), Ni_5P_4@C (b), and NiP_2@C (c) nanocomposites

The morphologies of the prepared Ni_xP_y@C nanocomposites are observed by SEM. As shown in Fig. 3a˜c, all prepared Ni_xP_y@C nanocomposites, Ni_2P@C, N_5P_4@C, and NiP_2@C, exhibit agglomerated sphere-like morphology. A lot of slit-like macropores which are caused by the unordered agglomeration of the sphere-like structure are observed, these macropores can provide fast channels for electrolyte ions during the fast charging/discharging process. The sample Ni_2P@C obtained at 300°C exhibits an average particle size of ca 80 nm, while that for N_5P_4@C and NiP_2@C reaches ca 190 and 270 nm. The size of the prepared Ni_xP_y@C nanocomposites increases apparently with the improving synthesizing temperature because the thickness of the carbon shell increase under high synthesizing temperature. the catalytic activity of Ni_xP_y nanoparticles to the dehydrogenation of PHAs coated on the surface of the Ni_xP_y nanoparticles enhances with the improving synthesizing temperature, which accelerates the carbonization of PHAs and then causes the augmentation of the size of the prepared nanocomposites. As shown in Fig. 3d˜i, the TEM images of the prepared Ni_xP_y@C nanocomposites proved that the Ni_2P, Ni_5P_4, and NiP_2nanoparticles with a size of 5˜15 nm are tightly coated by porous amorphous carbon. The developed pores in the amorphous carbon provide channels for electrolyte ions to conveniently reach the surface of the Ni_xP_y nanoparticles. Meanwhile, the high-magnification TEM images clearly show a lattice spacing of 0.25 nm for the (200) plane of the hexagonal Ni_2P, 0.22 nm for the (211) plane of the hexagonal Ni_5P_4, and 0.18 nm for the (221) plane of the cubic NiP_2 (insets in Fig. 3g˜i), which values are very close to the corresponding data in JCPDS cards NO. 074-1385 (Ni_2P), No. 18-0883 (Ni_5P_4) and No. 73-0436 (NiP_2). Furthermore, the EDS elemental mapping confirms the uniform distribution of Ni, P, and C elements in the obtained Ni_2P@C, N_5P_4@C, and NiP_2@C nanocomposites (Fig. 3j˜l).

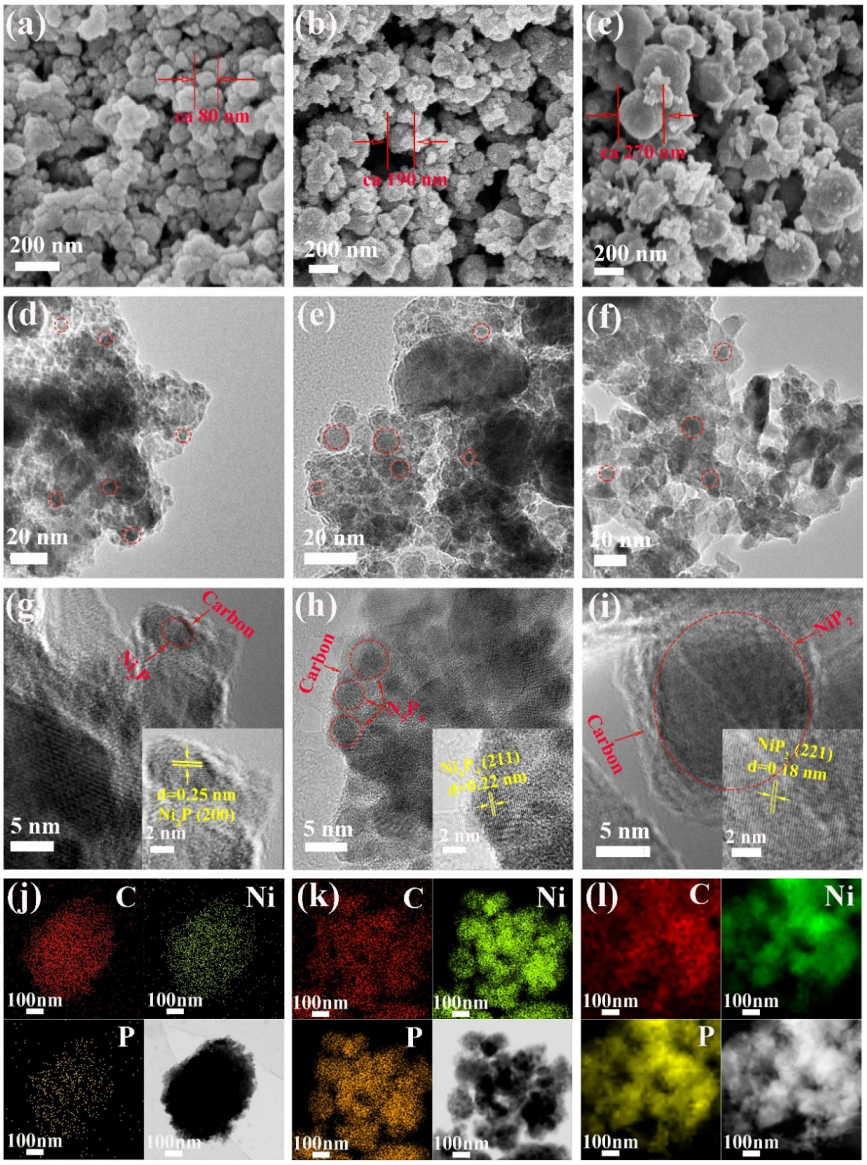

Fig. 3 SEM images of the prepared Ni_2P@C (a), N_5P_4@C (b), and NiP_2@C (c) nanocomposites; TEM images of the prepared Ni_2P@C (d), N_5P_4@C (e), and NiP_2@C (f) nanocomposites; HRTEM images of the prepared Ni_2P@C (g), N_5P_4@C (h), and NiP_2@C (i) nanocomposites, EDS elemental mapping images of the prepared Ni_2P@C (j), N_5P_4@C (k), and NiP_2@C (l) nanocomposites

The BET specific surface area of the prepared Ni_2P@C, Ni_5P_4@C, and NiP_2@C nanocomposites calculated according to the N_2adsorption/desorption isotherm reach 26.6 m^2g^{-1}, 20.2 m^2 g^{-1}, and 18.3 m^2 g^{-1}, respectively. The increased size of the prepared Ni_xP_y@C nanocomposites with the rising synthesizing temperature is responsible for the reduced specific surface area. The high specific surface area is conducive to enlarging the contact surface of the electrode materials with the electrolyte, thus boosting the electrochemical performance of the prepared materials. All Ni_xP_y@C nanocomposites display type-III N_2 adsorption/desorption isotherm with an H3-type hysteresis loop, as shown in Fig. 4a˜c. The hysteresis loop in N_2adsorption/desorption isotherm always indicates the existence of abundant mesopores [42]. The sharp increase of the N_2 adsorption quantity at the relative pressure of closing to 1.0 is generally caused by the macropores, which generate from

the aggregation of the Ni_xP_y@C nanocomposites while the mesopores originate from the porous amorphous carbon coating on the surface of the Ni_xP_y nanoparticles. The pore size distribution curves of the prepared Ni_xP_y@C nanocomposites further illuminate the co-existence of the mesopores and macropores. A balance pore size distribution of macropores and mesopores is revealed for the nanocomposite Ni_2P@C in the range from 2~150 nm, while macropore is found to be the dominant pore size distribution for the nanocomposites Ni_5P_4@C, and NiP_2@C. Meanwhile, an apparent increase in the average pore size with the rising synthesizing temperature can be observed.

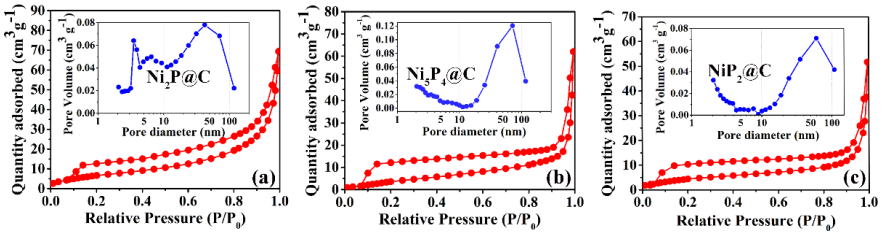

Fig. 4 N_2 adsorption-desorption curves and pore size distribution of prepared Ni_2P@C (a), Ni_5P_4@C (b), and NiP_2@C (c) nanocomposites

The surface element composition and valence bond configuration of the prepared Ni_xP_y@C nanocomposites are studied by XPS. As shown in Fig. 5a, Ni, P, C, and O elements are detected on the surfaces of the prepared Ni_2P@C, Ni_5P_4@C, and NiP_2@C nanocomposites. All high-resolution XPS spectra of Ni 2p orbits of all prepared Ni_xP_y@C nanocomposites display two pairs of spin orbits (Ni 2p1/2, Ni 2p3/2) and two satellite peaks ("Sat."), as shown in Fig. 5b. For the Ni_2P@C nanocomposite, the deconvolved peaks at 874.4 and 870.7 eV respectively correspond to the Ni 2p1/2 orbit of Ni^{3+} and Ni^{2+} while the peaks at 856.5 and 853.5 eV refer to Ni 2p3/2 orbit of Ni^{3+} and Ni^{2+}, respectively [43]. The orbital bond energies of Ni 2p1/2 orbit in Ni_5P_4@C nanocomposite shift to 874.6 and 871.0 eV while that of Ni 2p3/2 orbit transfer to 856.7 and 853.9 eV [44]. For NiP_2@C nanocomposite, the orbital bond energies of Ni 2p1/2 of $Ni^{\delta+}$ further move to 874.9 and 872.0 eV while that of Ni 2p3/2 orbit continually shifts to 856.8 and 854.7 eV. It can be seen that the orbital bond energies of Ni 2p1/2 and Ni 2p3/2 orbits in the prepared Ni_xP_y@C nanocomposites positively move to higher energy with the improved atomic ratio of P: Ni. Oppositely, a negative shift of the orbital bond energy is observed for the P 2p orbit. As shown in Fig. 5c, all high-resolution P 2p orbits of the prepared Ni_xP_y@C nanocomposites consist of three peaks corresponding to the P 2p1/2 and P 2p3/2 orbits in the P-Ni bond and the oxidized P species (133.8 eV)[38]. The orbital bond energy of the P 2p1/2 orbit locates at 132.3, 130.9, and 129.8 eV while that of the P 2p3/2 orbit centers at 129.8, 129.7, and 129.0 eV in the Ni_2P@C, Ni_5P_4@C, and NiP_2@C nanocomposites, respectively [17]. The results further confirm the successful synthesis of the Ni_2P@C, Ni_5P_4@C, and NiP_2@C nanocomposites by facilely adjusting the synthesizing temperature.

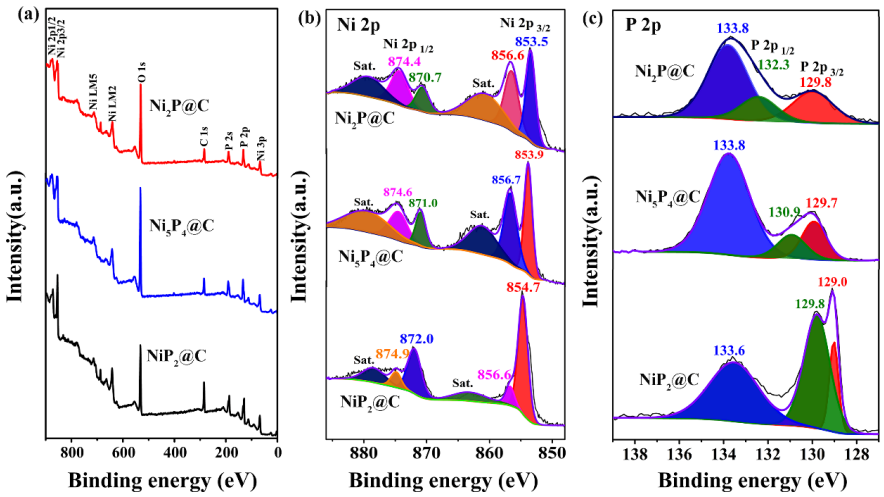

Fig. 5 survey XPS spectra of the prepared Ni_xP_y@C nanocomposites (a), core-level Ni 2p (b) and P 2p (c) orbits of the prepared Ni_xP_y@C nanocomposites

The electrochemical properties of the obtained Ni_xP_y@C nanocomposites are evaluated under a three-electrode configuration in 6 M KOH electrolyte. Apparent redox peaks can be observed from the CV curves of the prepared Ni_xP_y@C nanocomposites (Fig. 6a~c), revealing the dominant contribution of the pseudocapacitance to the charge storage capability of the prepared nanocomposites. Generally, the redox peaks of the Ni_xP_y are induced by the reversible transition of Ni^{2+}/Ni^{3+} redox couples [30]. The possible charge storage/release mechanism of the prepared Ni_xP_y@C nanocomposites in alkaline electrolyte follows the formula[45]:

$Ni_xP_y + OH^- - Ni_xP_y(OH) + e^-$ (6)

$Ni_xP_y(OH) + OH^- - Ni_xP_yO + H_2O + e^-$ (7)

Although the oxidation peaks occur right shift with the rising scan rate while a left shift is found for the reduction peaks, integral redox peaks still can be observed at a scan rate of 20 mV s^{-1}, indicating the fast charge transfer kinetics during the charging/discharging process of the prepared nanocomposites. For further comprehending the charge transfer kinetics, the formula $\log(i) = b\log(v) + \log(a)$ is utilized to investigate the relationship between scanning rate (v) and peak current response (i). By linear fitting the graph of $\log(i)$ vs $\log(v)$, the value of the coefficients $a$and b can be obtained. The value of coefficient $b$generally reflects the charge transfer kinetics mechanism of electrode material [42]. A value of closing to 1.0 indicates the energy storage generated from the surface–controlled process while the semi-infinite diffusion-controlled Faraday process is recommended by ab value of closing to 0.5 [45,46]. As shown in Fig.6d, the b values of the nanocomposites Ni_2P@C, Ni_5P_4@C, and NiP_2@C reach 0.621, 0.722, and 0.730, indicating a co-contribution from the surface–controlled and diffusion-controlled process to the charge transfer process of the Ni_xP_y@C nanocomposites. A higher b value is found for the nanocomposite NiP_2@C than that of the nanocomposites Ni_2P@C and Ni_5P_4, indicating a larger contribution from the surface–controlled process for the nanocomposite NiP_2@C. The capacitance contribution from the surface–controlled and the diffusion-controlled process can be further quantified by the formula [46]. In this formula, k_1 and $k_2$are linear fitting constants, which can be obtained by the slope and intercept of the linear equation, $k_1 v$ and$k_2 v^{1/2}$ correspond to the current contribution derived from the surface–controlled and diffusion-controlled processes, respectively. As shown in Fig. 6e and Fig. S1, the capacitance contribution from the surface–controlled process achieves 12.23%, 16.99%, and 23.22% for the nanocomposites Ni_2P@C, Ni_5P_4@C, and NiP_2@C at a scan rate of 5mV s^{-1}, respectively. These results illuminate the diffusion-controlled process dominated charge storage mechanism for the prepared Ni_xP_y@C nanocomposites, which is the typical characteristic of the battery-like electrode materials. With the rising scan rate from 1 to 20 mV s^{-1}, the capacitance

contribution from the surface–controlled process improves from 19.71% to 37.86% for the nanocomposite NiP_2@C while that for nanocomposites Ni_2P@C and Ni_5P_4@C increases from 10.04% and 10.73% to 30.28% and 29.64%, respectively (Fig. 6f and Fig. S2). The nanocomposite NiP_2@C exhibits a higher surface–controlled contribution for energy storage than the nanocomposites Ni_2P@C and Ni_5P_4@C under various scan rates, indicating its better rate capability than other samples.

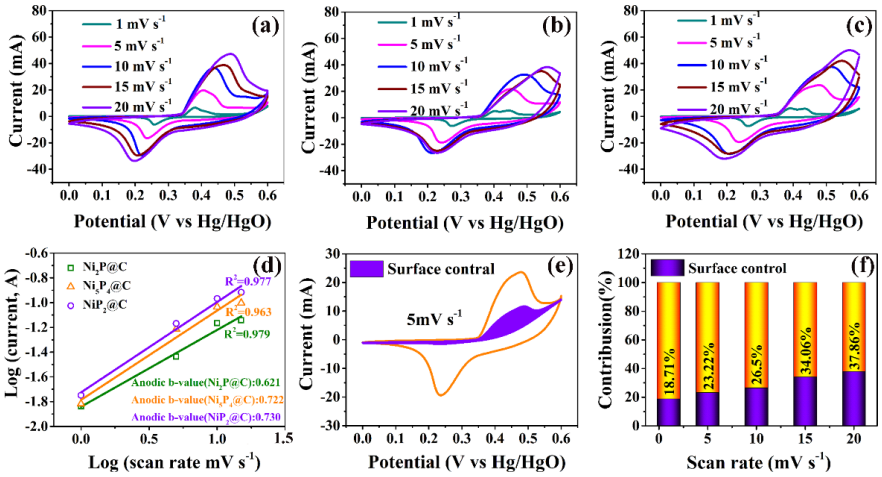

Fig. 6 CV curves of the prepared Ni_2P@C (a), Ni_5P_4@C (b), and NiP_2@C (c) nanocomposites; b value of the prepared Ni_xP_y@C nanocomposites (d); contribution of surface-controlled process at a scan rate of 5 mV s^{-1} for the nanocomposite NiP_2@C (e), and columnar contribution map of surface-controlled process at different scan rates for the nanocomposite NiP_2@C (f)

Fig. 7a compares the CV curves of the prepared Ni_xP_y@C nanocomposites at a scan rate of 5 mV s^{-1}. Although all nanocomposites exhibit similar CV curves, the CV curve of nanocomposite NiP_2@C shows a larger coverage area and higher redox peaks than nanocomposites Ni_2P@C and Ni_5P_4@C, indicating the higher charge storage capacity of the nanocomposite NiP_2@C than others. Fig. 7b and Fig. S3 present the GCD curves of the prepared Ni_xP_y@C nanocomposites at a current density of 1 A g^{-1}. It can be seen that the discharge time of the nanocomposite NiP_2@C is significantly longer than that of other nanocomposites, indicating its larger specific capacity, which result is in good agreement with the result from CV curves. The GCD curves of the nanocomposite NiP_2@C at different current densities are shown in Fig. 6c. A typical symmetrical charge-discharge plateau can be observed even under a current density of 10 A g^{-1}, indicating its reversible redox reaction-based energy storage mechanism and good reversibility. The specific capacities of the nanocomposite NiP_2@C achieve 197.2, 164.9, 135.7, and 109.8 mAh g^{-1} at current densities of 1, 2, 5, and 10 A g^{-1}, respectively. More than 55.68% of the initial capacity is retained as the current density increases from 1 to 10 A g^{-1}. Specific capacities of the nanocomposites Ni_2P@C and Ni_5P_4@C reach 156.5 and 187.2 mAh g^{-1} at the current density of 1 A g^{-1}, while those values retain at 81.1 and 77.1 mAh g^{-1} at 10 A g^{-1}, respectively. The nanocomposite NiP_2@C exhibits higher specific capacity and better rate performance than the nanocomposites Ni_2P@C and Ni_5P_4@C (Fig. 7d). Compared with other nickel-based phosphides and their composites reported in the literature, the obtained Ni_xP_y@C nanocomposites prepared by the newly developed SPS method are more competitive[17,18,25,38,43-50], as shown in Table 1.

Table 1 Specific capacity metrics of various nickel-based phosphides and their composites

Materials	*Specific capacity*	*Reference*
Ni_2P/Ni/C composites	71.4 mAh g^{-1} at 1 A g^{-1}	[38]

Materials	*Specific capacity*	*Reference*
rGO/Ni_2P composite	123.6 mAh g^{-1} at 1 A g^{-1}	[47]
Ni_2P-CNFs composite	145 mAh g^{-1} at 0.5 A g^{-1}	[43]
$Ni_2P/Ni_{12}P_5$ composite	147.3 mAh g^{-1} at 1 A g^{-1}	[48]
Coral–like Ni_2P@C composite	135.9 mAh g^{-1} at 1 A g^{-1}	[17]
$Ni_xCo_{1-x}P$ hollow nanocages	152.2 mAh g^{-1} at 1 A g^{-1}	[44]
1D NiCoP nanowire	193.7 mAh g^{-1} at 1 A g^{-1}	[49]
3D hollow NiCoP microcubes	174.7 mAh g^{-1} at 1 A g^{-1}	[45]
	181.4 mAh g^{-1} at 1 A g^{-1}	[46]
3D NiCoP heterostructure		
	220.8 mAh g^{-1} at 1 A g^{-1}	[50]
Hollow NiCoP nanocubes		
NiCoP hollow nanocubes	182.9 mAh g^{-1} at 1 A g^{-1}	[25]
$Ni_{12}P_5$ nanowires	196.4 mAh g^{-1} at 1 A g^{-1}	[18]
Ni_2P@C nanocomposite	156.5 mAh g^{-1} at 1 A g^{-1}	This work
Ni_5P_4@C nanocomposite	187.2 mAh g^{-1} at 1 A g^{-1}	
NiP_2@C nanocomposite	197.2 mAh g^{-1} at 1 A g^{-1}	

Electrochemical impedance spectroscopy (EIS) under the frequency range from 0.01Hz˜100kHz is tested to comprehend the conductive and diffusive behaviors of the prepared Ni_xP_y@C nanocomposites. The straight line in the low-frequency region in the Nyquist plot represents the Warburg impedance while the slope represents the diffusion resistance of the electrolyte ions in the microscopic pore structure of the electrode material [29]. A straight line in the low-frequency region perpendicular to the x-axis indicates the ideal capacitance characteristic of the electrode materials. As shown in Fig. 7e, a straight line nearly perpendicular to the x-axis is observed for all nanocomposites, indicating their good capacitance characteristics. The intercept of the x-axis of the Nyquist plot represents the equivalent series resistance (Rs) of the electrode material and electrolyte, while the semicircle in the high-frequency region corresponds to the charge transfer resistance (Rct) [28]. The similar semicircles with close diameters in the high-frequency region demonstrate their very close charge transfer resistance. All prepared nanocomposites exhibit low equivalent series resistance, the Rs values for nanocomposites Ni_2P@C, Ni_5P_4@C, and NiP_2@C are 0.69, 0.66, and 0.65 Ω. The low Rs and Rct values illuminate the good conductivity of the prepared nanocomposites. Fig. 7f displays the cycle performance of the prepared nanocomposites in the three-electrode system. After 1000 cycles at a current density of 7A g^{-1}, more than 84.3% of the initial specific capacity is retained for the nanocomposite NiP_2@C, while that value for the nanocomposites Ni_2P@C and Ni_5P_4@C reaches 73.81% and 82.81%, respectively. The prepared nanocomposites exhibit satisfactory cycle stability, especially for the nanocomposite NiP_2@C.

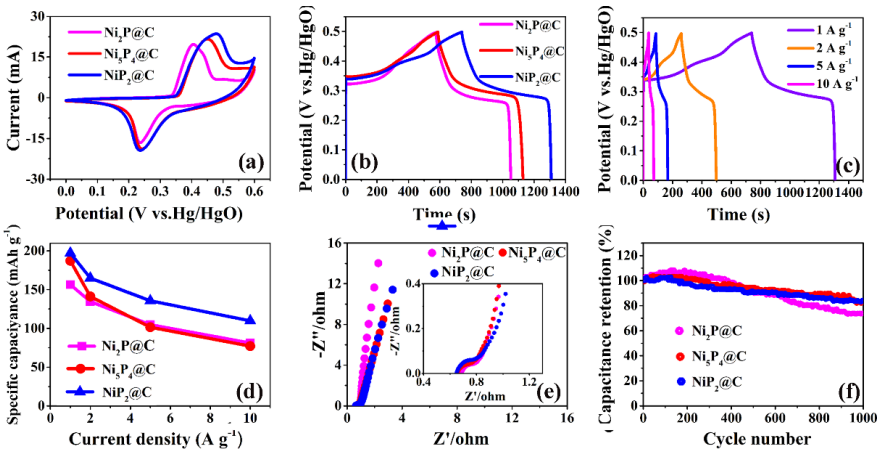

Fig. 7 CV curves at a scan rate of 5 mV s^{-1}(a) and GCD curves at a current density of 1 A g^{-1} (b) of the prepared Ni_xP_y@C nanocomposites; GCD curves of the nanocomposite NiP_2@C under different current densities (c); specific capacitance of the prepared Ni_xP_y@C nanocomposites under different current densities (d); Nyquist plots of the prepared Ni_xP_y@C nanocomposites (e); cycle performance of the prepared Ni_xP_y@C nanocomposites

To further evaluate the application potential of the prepared Ni_xP_y@C nanocomposites in supercapacitor devices, hybrid supercapacitor devices (Ni_xP_y@C//IHPC) are assembled by using the prepared Ni_xP_y@C nanocomposites as the positive electrode active material and an interconnected hierarchical porous carbon (IHPC) reported in our previous work as the negative electrode active material. The negative electrode active material (IHPC) exhibits interconnected hierarchical morphology with an ultra-high specific surface area as high as 3463 m^2g^{-1} and high conductivity of 8.7 S cm^{-1}, which specific capacitance achieves 445 F g^{-1} at a current density of 0.5 A g^{-1}, and more than 89% of the initial specific capacitance is retained even under a high current density of 20 A g^{-1} [39]. The morphology, N_2 adsorption/desorption isotherm, and main electrochemical properties are presented in Fig. S4. The working voltage window of the IHPC is -1.0 – 0 V, while the stable working voltage window of the obtained Ni_xP_y@C nanocomposites is 0 – 0.6 V (Fig. 8a). Therefore, the theoretical maximum operating voltage of the assembled HSC is as high as 1.6 V. The CV curves of the assembled HSCs within the voltage window of 0 - 1.6 V are shown in Fig. 8b. No obvious polarization is observed under the voltage window of 0 - 1.6 V for the assembled Ni_xP_y@C//IHPC devices, indicating the stable operation of the assembled HSCs at 1.6 V. Under the same scan rate, the CV curve of the device NiP_2@C//IHPC shows a larger coverage area than the devices Ni_2P@C//IHPC and Ni_5P_4@C//IHPC, indicating a better charge storage capacity for the device NiP_2@C//IHPC than others. The GCD curves of the assembled Ni_xP_y@C//IHPC devices at a current density of 1 A g^{-1} conform to typical characteristics of hybrid capacitors, as shown in Fig. 8c. Fig. 8d~f displays the GCD curves of the assembled Ni_xP_y@C//IHPC devices under different current densities. The symmetry of the GCD curves is perfectly maintained even under a current density of 10 A g^{-1}, illuminating the good capacitive performance and high coulomb efficiency of the assembled Ni_xP_y@C//IHPC devices. The specific capacities of the assembled Ni_xP_y@C//IHPC devices under different current densities are presented in Fig. 8g. The specific capacities of the devices Ni_2P@C//IHPC, Ni_5P_4@C//IHPC, and NiP_2@C//IHPC achieve 59.9, 55.9, and 63.0 mAh g^{-1} at a current density of 1 A g^{-1}, which values still keep at 18.8, 33.2, and 38.4 mAh g^{-1} for the corresponding devices as the current density increases tenfold, the specific capacity retention reaches 31.4, 59.3, and 60.1% for the devices Ni_2P@C//IHPC, Ni_5P_4@C//IHPC, and NiP_2@C//IHPC respectively. The device NiP_2@C//IHPC exhibits higher specific capacity and better rate capability than others. After 20000 cycles at a current density of 7 A g^{-1}, more than 84.7%, 87.7%, and 83.8% of initial specific capacity are retained for the device Ni_2P@C//IHPC, Ni_5P_4@C//IHPC, and NiP_2@C//IHPC (Fig. 8f), respectively, proving their good electrochemical reversibility and cycle stability. The quantitative relationship between specific energy and specific power of the assembled HSC devices is shown in Fig. 8i. The device NiP_2@C//IHPC delivers

a desirable energy density of 50.38 Wh kg^{-1} at a specific power of 0.89 kW kg^{-1}, and which value can still reach 29.1 Wh kg^{-1} at a large power density of 9.44 kW kg^{-1}, while relatively low specific energy of 47.94 and 44.67 Wh kg^{-1} is delivered at specific power of 1.01 and 0.95 kW kg^{-1} for the devices Ni_2P@C//IHPC and Ni_5P_4@C//IHPC, respectively. The energy density of the assembled Ni_xP_y@C//IHPC devices outperforms other HSCs based on nickel-based phosphide and their nanocomposites, such as Ni_2P/Ni/C//PC (25.4 Wh kg^{-1} at 0.75 kW kg^{-1})[38], rGO/Ni_2P//AC (35.9 W h kg^{-1} at 752 W kg^{-1})[47], Ni_2P-CNFs//CNFs (42 Wh kg^{-1} at 413 W kg^{-1})[43], NiCoP nanoplates//graphene (32.9 Wh kg^{-1} at 1.3 kW kg^{-1})[51], coral–like Ni_2P@C//AC (44.0 Wh kg^{-1} at 800 W kg^{-1})[17], NiCuP//BAC(40.5 W h kg^{-1} at 875 W kg^{-1}) [52], CoP@NiCoP/NF//Fe_2O_3 (37.16 Wh kg^{-1} at 875 W kg^{-1})[53], NiCoP@P-rGO//AC (39.7 Wh kg^{-1} at 875 W kg^{-1}) [54].

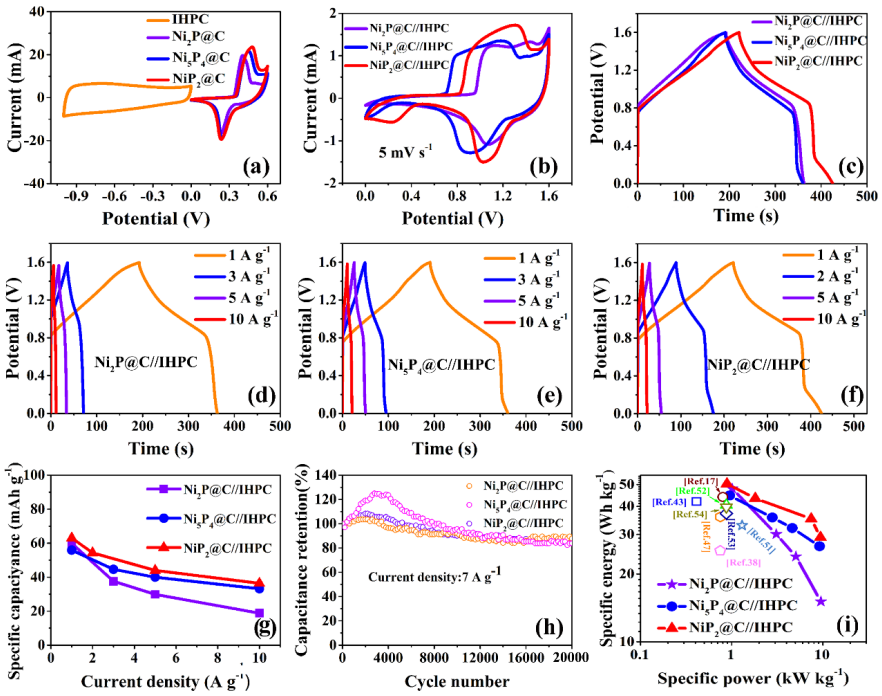

Fig. 8 CV curves of the positive and negative materials at a scan rate of 5 mV s^{-1} (a); CV curves of the assembled HSCs at a scan rate of 5 mV s^{-1} (b); GCD curves of the assembled HSCs at a current density of 1 A g^{-1} (c); GCD curves of the assembled HSCs (d~f) at different densities; specific capacity of the assembled HSCs under different current densities (g); 20000 cycle performance of the assembled HSC (h); Ragone plot of the assembled HSCs (i)

4. Conclusions

A convenient and efficient one-step solid-phase synthesis method is successfully developed for the preparation of Ni_xP_y@C nanocomposites. By controlling the synthesizing temperature, Ni_2P@C, Ni_5P_4@C, and NiP_2@C nanocomposites can be facilely synthesized under an ambient atmosphere. The solid-phase synthesized Ni_xP_y@C nanocomposites exhibit high charge storage capability and good cycle stability. A high specific capacity of over 197.2 mAh g^{-1} is achieved at a current density of 1 A g^{-1} for the optimal nanocomposite NiP_2@C, and more than 84.3% of initial specific capacitance is kept after 1000 cycles. The assembled hybrid supercapacitor device based on the nanocomposite NiP_2@C and an interconnected hierarchical porous carbon (NiP_2@C//IHPC) delivers a specific energy of up to 50.38 Wh kg^{-1} at a specific power of 0.89 kW kg^{-1}, which value still reaches 29.1 Wh kg^{-1} at a high specific power of 9.44 kW kg^{-1}. More than 83.8% of initial specific capacity is retained after 20000 cycles. Compared with the other nickel-based phosphides and their composites prepared by other methods, the prepared Ni_xP_y@C nanocomposites by the developed one-step

SPS method demonstrate very competitive performance with the distinguished merits of convenient, efficient, target-oriented, cost-efficiency, and eco-friendly. The successfully developed solid-phase synthesis method is proved to be a reliable strategy for facile preparation of TMPs with high performance.

Acknowledgment

This work was supported by the National Natural Science Foundation of China (Grant No. 52162031 and 21867015) and the Natural Science Foundation of Gansu Province in China (Grant No. 20JR10RA155).

References

1. Hussain I, Iqbal S, Lamiel C, Alfantazi A, Zhang K. Recent advances in oriented metal–organic frameworks for supercapacitive energy storage. *Journal of Materials Chemistry A.* 2022;10(9):4475-4488.

2. Chen S, Qiu L, Cheng H-M. Carbon-Based Fibers for Advanced Electrochemical Energy Storage Devices. *Chemical Reviews.*2020/03/11 2020;120(5):2811-2878.

3. Kumar S, Saeed G, Zhu L, Hui KN, Kim NH, Lee JH. 0D to 3D carbon-based networks combined with pseudocapacitive electrode material for high energy density supercapacitor: A review. *Chemical Engineering Journal.* 2021/01/01/ 2021;403:126352.

4. Xiao J, Han J, Zhang C, Ling G, Kang F, Yang Q-H. Dimensionality, Function and Performance of Carbon Materials in Energy Storage Devices.*Advanced Energy Materials.* 2022;12(4):2100775.

5. Luo X-y, Chen Y, Mo Y. A review of charge storage in porous carbon-based supercapacitors. *New Carbon Materials.* 2021/02/01/ 2021;36(1):49-68.

6. Choudhary RB, Ansari S, Majumder M. Recent advances on redox active composites of metal-organic framework and conducting polymers as pseudocapacitor electrode material. *Renewable and Sustainable Energy Reviews.* 2021/07/01/ 2021;145:110854.

7. Zhu X. Recent advances of transition metal oxides and chalcogenides in pseudo-capacitors and hybrid capacitors: A review of structures, synthetic strategies, and mechanism studies. *Journal of Energy Storage.* 2022/05/01/ 2022;49:104148.

8. Chatterjee DP, Nandi AK. A review on the recent advances in hybrid supercapacitors. *Journal of Materials Chemistry A.*2021;9(29):15880-15918.

9. Chodankar NR, Pham HD, Nanjundan AK, et al. True Meaning of Pseudocapacitors and Their Performance Metrics: Asymmetric versus Hybrid Supercapacitors. *Small.* 2020;16(37):2002806.

10. Wang J, Zhang D, She W, et al. Flower-like NiCo-carbonate Hydroxides for High-performance Solid-state Hybrid Supercapacitor.*Electroanalysis.* n/a(n/a).

11. Ambade RB, Lee H, Hyun Lee K, et al. Ultrafast flashlight sintered mesoporous NiO nanosheets for stable asymmetric supercapacitors.*Chemical Engineering Journal.* 2022/05/15/ 2022;436:135041.

12. Bounor B, Asbani B, Douard C, Favier F, Brousse T, Lethien C. On chip MnO2-based 3D micro-supercapacitors with ultra-high areal energy density. *Energy Storage Materials.* 2021/06/01/ 2021;38:520-527.

13. Chen S, Jiang H, Cheng Q, Wang G, Petr S, Li C. Amorphous vanadium oxides with metallic character for asymmetric supercapacitors.*Chemical Engineering Journal.* 2021/01/01/ 2021;403:126380.

14. Delbari SA, Ghadimi LS, Hadi R, et al. Transition metal oxide-based electrode materials for flexible supercapacitors: A review.*Journal of Alloys and Compounds.* 2021/03/15/ 2021;857:158281.

15. Liu R, Zhou A, Zhang X, et al. Fundamentals, advances and challenges of transition metal compounds-based supercapacitors. *Chemical Engineering Journal.* 2021/05/15/ 2021;412:128611.

16. Zong Q, Liu C, Yang H, Zhang Q, Cao G. Tailoring nanostructured transition metal phosphides for high-performance hybrid supercapacitors.*Nano Today.* 2021/06/01/ 2021;38:101201.

17. Aziz SKT, Kumar S, Riyajuddin S, Ghosh K, Nessim GD, Dubal DP. Bimetallic Phosphides for Hybrid Supercapacitors. *The Journal of Physical Chemistry Letters.* 2021/06/03 2021;12(21):5138-5149.

18. Shi Y, Li M, Yu Y, Zhang B. Recent advances in nanostructured transition metal phosphides: synthesis and energy-related applications.*Energy & Environmental Science.* 2020;13(12):4564-4582.

19. Xu F, Xia Q, Du G, Fan Z, Chen N. Coral–like Ni2P@C derived from metal–organic frameworks with superior electrochemical performance for hybrid supercapacitors. *Electrochimica Acta.* 2021/06/01/ 2021;380:138200.

20. Gan Y, Wang C, Chen X, et al. High conductivity Ni12P5 nanowires as high-rate electrode material for battery-supercapacitor hybrid devices.*Chemical Engineering Journal.* 2020/07/15/ 2020;392:123661.

21. Liu S, Sankar KV, Kundu A, Ma M, Kwon J-Y, Jun SC. Honeycomb-Like Interconnected Network of Nickel Phosphide Heteronanoparticles with Superior Electrochemical Performance for Supercapacitors. *ACS Applied Materials & Interfaces.* 2017/07/05 2017;9(26):21829-21838.

22. Zhang Q, Zhang W-B, Hei P, Hou Z, Yang T, Long J. CoP nanoprism arrays: Pseudocapacitive behavior on the electrode-electrolyte interface and electrochemical application as an anode material for supercapacitors. *Applied Surface Science.* 2020/10/15/ 2020;527:146682.

23. Sun L, Xie Z, Wu A, et al. Hollow CoP spheres assembled from porous nanosheets as high-rate and ultra-stable electrodes for advanced supercapacitors. *Journal of Materials Chemistry A.*2021;9(46):26226-26235.

24. Chodankar NR, Shinde PA, Patil SJ, et al. Solution-free self-assembled growth of ordered tricopper phosphide for efficient and stable hybrid supercapacitor. *Energy Storage Materials.*2021/08/01/ 2021;39:194-202.

25. Liu W, Gao H, Zhang Z, et al. CoP/Cu3P heterostructured nanoplates for high-rate supercapacitor electrodes. *Chemical Engineering Journal.* 2022/06/01/ 2022;437:135352.

26. Zhu Y, Lu P, Li F, Ding Y, Chen Y. Metal-Rich Porous Copper Cobalt Phosphide Nanoplates as a High-Rate and Stable Battery-Type Cathode Material for Battery–Supercapacitor Hybrid Devices. *ACS Applied Energy Materials.* 2021/04/26 2021;4(4):3962-3974.

27. Li P, Zhang M, Yin H, Yao J, Liu X, Chen S. Hierarchical mesoporous NiCoP hollow nanocubes as efficient and stable electrodes for high-performance hybrid supercapacitor. *Applied Surface Science.*2021/01/15/ 2021;536:147751.

28. Wan L, Wang Y, Zhang Y, et al. Designing FeCoP@NiCoP heterostructured nanosheets with superior electrochemical performance for hybrid supercapacitors. *Journal of Power Sources.* 2021/09/15/ 2021;506:230096.

29. Cao L-M, Zhang J, Ding L-W, Du Z-Y, He C-T. Metal-organic frameworks derived transition metal phosphides for electrocatalytic water splitting. *Journal of Energy Chemistry.* 2022/05/01/ 2022;68:494-520.

30. Zhang D, Gao S, Zhang J, et al. Facile solid-phase synthesis of layered NiS/rGO nanocomposite for high-performance hybrid supercapacitor. *Journal of Power Sources.* 2021/12/01/ 2021;514:230590.

31. Zhang J, Zhang D, Yang B, et al. Targeted synthesis of NiS and NiS2 nanoparticles for high-performance hybrid supercapacitor via a facile green solid-phase synthesis route. *Journal of Energy Storage.*2020/12/01/ 2020;32:101852.

32. Li X, Ma J, Luo J, et al. Porous N, P co-doped carbon-coated ultrafine Co2P nanoparticles derived from DNA: An electrocatalyst for highly efficient hydrogen evolution reaction. *Electrochimica Acta.* 2021/10/10/

2021;393:139051.

33. Yang B, Zhang D, She W, et al. Remarkably improving the specific energy of supercapacitor based on a biomass-derived interconnected hierarchical porous carbon by using a newly-developed mixed alkaline aqueous electrolyte with widened operation voltage. *Journal of Power Sources.* 2021/04/30/ 2021;492:229666.

34. Xia B, Lenggoro IW, Okuyama K. Preparation of Nickel Powders by Spray Pyrolysis of Nickel Formate. *Journal of the American Ceramic Society.* 2001;84(7):1425-1432.

35. Wender PA, Smith TE. Tetrakis(triphenylphosphine)nickel(0).*Encyclopedia of Reagents for Organic Synthesis* .

36. Wei J, Ni Y, Xiang N, Zhang Y, Ma X. Urchin-like NixPy hollow superstructures: mild solvothermal synthesis and enhanced catalytic performance for the reduction of 4-nitrophenol. *CrystEngComm.*2014;16(11):2113-2118.

37. Peng C-Y, Kang L, Cao S, Chen Y, Lin Z-S, Fu W-F. Nanostructured Ni2P as a Robust Catalyst for the Hydrolytic Dehydrogenation of Ammonia–Borane. *Angewandte Chemie International Edition.*2015;54(52):15725-15729.

38. Xu Y, Xiong S, Weng S, et al. Rationally designed Ni2P/Ni/C as a positive electrode for high-performance hybrid supercapacitors.*New Journal of Chemistry.* 2020;44(17):6810-6817.

39. Ye J, Xia G, Yang X, et al. Ultrafine Ni5P4 nanoparticles embedded in 3D porous carbon foams for high-performance lithium-ion and potassium-ion batteries. *Journal of Alloys and Compounds.*2022/01/25/ 2022;891:161951.

40. Li X, Wang R, Yu Y, et al. MOF-derived Multi-Shelled NiP2 Microspheres as High-Performance Anode Materials for Sodium-/Potassium-Ion Batteries. *Advanced Energy and Sustainability Research.* 2022/03/23 2022;n/a(n/a):2200010.

41. Li Y, Zhang D, Han M, et al. Fabrication of the phosphorus doped mesoporous carbon with superior capacitive performance by microwave irradiation under ambient atmosphere: An ultra-facile and energy-efficient method. *Applied Surface Science.* 2018/11/15/ 2018;458:119-128.

42. Zhang D, Yang B, She W, et al. Simultaneously achieving high energy and power density for ultrafast-charging supercapacitor built by a semi-graphitic hierarchical porous carbon nanosheet and a high-voltage alkaline aqueous electrolyte. *Journal of Power Sources.*2021/09/15/ 2021;506:230103.

43. Peng H, Zhou J, Chen Z, et al. Integrated carbon nanosheet frameworks inlaid with nickel phosphide nanoparticles by substrate-free chemical blowing and phosphorization for aqueous asymmetric supercapacitor. *Journal of Alloys and Compounds.* 2019/08/15/ 2019;797:1095-1105.

44. Xu Y, Hou S, Yang G, Wang X, Lu T, Pan L. Synthesis of bimetallic NixCo1-xP hollow nanocages from metal-organic frameworks for high performance hybrid supercapacitors. *Electrochimica Acta.*2018/09/20/ 2018;285:192-201.

45. Zhang X, Zhang L, Xu G, Zhao A, Zhang S, Zhao T. Template synthesis of structure-controlled 3D hollow nickel-cobalt phosphides microcubes for high-performance supercapacitors. *Journal of Colloid and Interface Science.* 2020/03/01/ 2020;561:23-31.

46. He S, Li Z, Mi H, et al. 3D nickel-cobalt phosphide heterostructure for high-performance solid-state hybrid supercapacitors. *Journal of Power Sources.* 2020/08/15/ 2020;467:228324.

47. Lv Z, Zhong Q, Bu Y. In-situ conversion of rGO/Ni2P composite from GO/Ni-MOF precursor with enhanced electrochemical property.*Applied Surface Science.* 2018/05/01/ 2018;439:413-419.

48. Xie S, Gou J. Facile synthesis of Ni2P/Ni12P5 composite as long-life electrode material for hybrid supercapacitor. *Journal of Alloys and Compounds.* 2017/08/05/ 2017;713:10-17.

49. Sivakumar P, Jung MG, Raj CJ, Rana HH, Park HS. 1D interconnected porous binary transition metal phosphide nanowires for high performance hybrid supercapacitors. *International Journal of Energy Research.*2021;45(11):17005-17014.

50. Wang M, Zhong J, Zhu Z, et al. Hollow NiCoP nanocubes derived from a Prussian blue analogue self-template for high-performance supercapacitors. *Journal of Alloys and Compounds.* 2022/02/10/ 2022;893:162344.

51. Liang H, Xia C, Jiang Q, Gandi AN, Schwingenschlögl U, Alshareef HN. Low temperature synthesis of ternary metal phosphides using plasma for asymmetric supercapacitors. *Nano Energy.* 2017/05/01/ 2017;35:331-340.

52. El Sharkawy HM, Sayed DM, Dhmees AS, Aboushahba RM, Allam NK. Facile Synthesis of Nanostructured Binary Ni–Cu Phosphides as Advanced Battery Materials for Asymmetric Electrochemical Supercapacitors. *ACS Applied Energy Materials.* 2020/09/28 2020;3(9):9305-9314.

53. Wang X, Jing C, Zhang W, et al. One-step phosphorization synthesis of CoP@NiCoP nanowire/nanosheet composites hybrid arrays on Ni foam for high-performance supercapacitors. *Applied Surface Science.*2020/12/01/ 2020;532:147437.

54. Javed U, Dhakal G, Rabie AM, et al. Heteroatom-doped reduced graphene oxide integrated with nickel-cobalt phosphide for high-performance asymmetric hybrid supercapacitors. *Materials Today Nano.* 2022/03/26/ 2022:100195.

Table captions

Table 1 Specific capacity metrics of various nickel-based phosphides and their composites

Materials	*Specific capacity*	*Reference*
Ni_2P/Ni/C composites	71.4 mAh g^{-1} at 1 A g^{-1}	[38]
rGO/Ni_2P composite	123.6 mAh g^{-1} at 1 A g^{-1}	[47]
Ni_2P-CNFs composite	145 mAh g^{-1} at 0.5 A g^{-1}	[43]
$Ni_2P/Ni_{12}P_5$ composite	147.3 mAh g^{-1} at 1 A g^{-1}	[48]
Coral–like Ni_2P@C composite	135.9 mAh g^{-1} at 1 A g^{-1}	[17]
$Ni_xCo_{1-x}P$ hollow nanocages	152.2 mAh g^{-1} at 1 A g^{-1}	[44]
1D NiCoP nanowire	193.7 mAh g^{-1} at 1 A g^{-1}	[49]
3D hollow NiCoP microcubes	174.7 mAh g^{-1} at 1 A g^{-1}	[45]
	181.4 mAh g^{-1} at 1 A g^{-1}	[46]
3D NiCoP heterostructure		
	220.8 mAh g^{-1} at 1 A g^{-1}	[50]
Hollow NiCoP nanocubes		
NiCoP hollow nanocubes	182.9 mAh g^{-1} at 1 A g^{-1}	[25]
$Ni_{12}P_5$ nanowires	196.4 mAh g^{-1} at 1 A g^{-1}	[18]
Ni_2P@C nanocomposite	156.5 mAh g^{-1} at 1 A g^{-1}	This work
Ni_5P_4@C nanocomposite	187.2 mAh g^{-1} at 1 A g^{-1}	

Materials	*Specific capacity*	*Reference*
NiP_2@C nanocomposite	197.2 mAh g^{-1} at 1 A g^{-1}	

Figure captions

Fig. 1 the scheme for the solid-phase synthesis of Ni_xP_y@C nanocomposites

Fig. 2 XRD spectra of the prepared NiP_2@C (a), Ni_5P_4@C (b), and NiP_2@C (c) nanocomposites

Fig. 3 SEM images of the prepared Ni_2P@C (a), N_5P_4@C (b), and NiP_2@C (c) nanocomposites; TEM images of the prepared Ni_2P@C (d), N_5P_4@C (e), and NiP_2@C (f) nanocomposites; HRTEM images of the prepared Ni_2P@C (g), N_5P_4@C (h), and NiP_2@C (i) nanocomposites, EDS elemental mapping images of the prepared Ni_2P@C (j), N_5P_4@C (k), and NiP_2@C (l) nanocomposites

Fig. 4 N_2 adsorption-desorption curves and pore size distribution of prepared Ni_2P@C (a), Ni_5P_4@C (b), and NiP_2@C (c) nanocomposites

Fig. 5 survey XPS spectra of the prepared Ni_xP_y@C nanocomposites (a), core-level Ni 2p (b) and P 2p (c) orbits of the prepared Ni_xP_y@C nanocomposites

Fig. 6 CV curves of the prepared Ni_2P@C (a), Ni_5P_4@C (b), and NiP_2@C (c) nanocomposites; b value of the prepared Ni_xP_y@C nanocomposites (d); contribution of surface-controlled process at a scan rate of 5 mV s^{-1} for the nanocomposite NiP_2@C (e), and columnar contribution map of surface-controlled process at different scan rates for the nanocomposite NiP_2@C (f).

Fig. 7 CV curves at a scan rate of 5 mV s^{-1}(a) and GCD curves at a current density of 1 A g^{-1} (b) of the prepared Ni_xP_y@C nanocomposites; GCD curves of the nanocomposite NiP_2@C under different current densities (c); specific capacitance of the prepared Ni_xP_y@C nanocomposites under different current densities (d); Nyquist plots of the prepared Ni_xP_y@C nanocomposites (e); cycle performance of the prepared Ni_xP_y@C nanocomposites

Fig. 8 CV curves of the positive and negative materials at a scan rate of 5 mV s^{-1} (a); CV curves of the assembled HSCs at a scan rate of 5 mV s^{-1} (b); GCD curves of the assembled HSCs at a current density of 1 A g^{-1} (c); GCD curves of the assembled HSCs (d~f) at different densities; specific capacity of the assembled HSCs under different current densities (g); 20000 cycle performance of the assembled HSC (h); Ragone plot of the assembled HSCs (i)

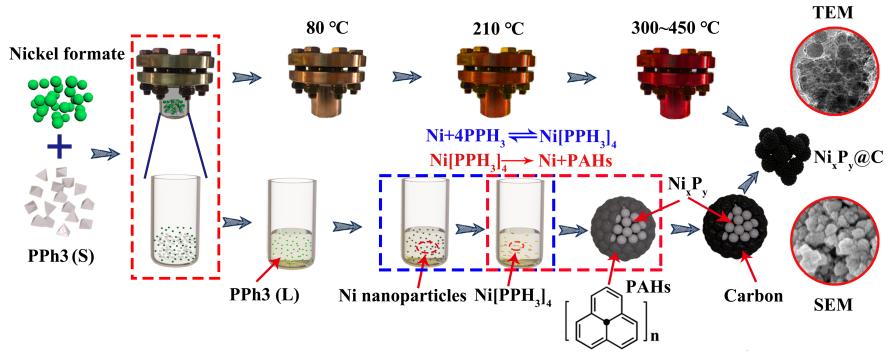

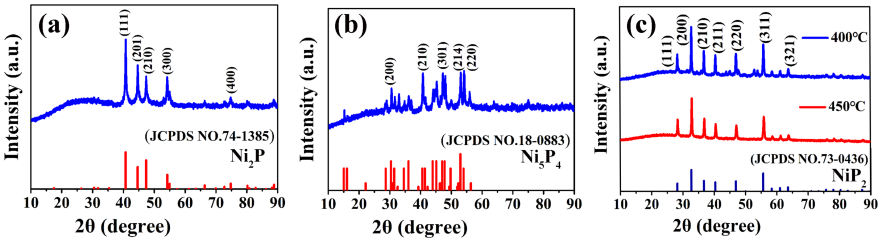

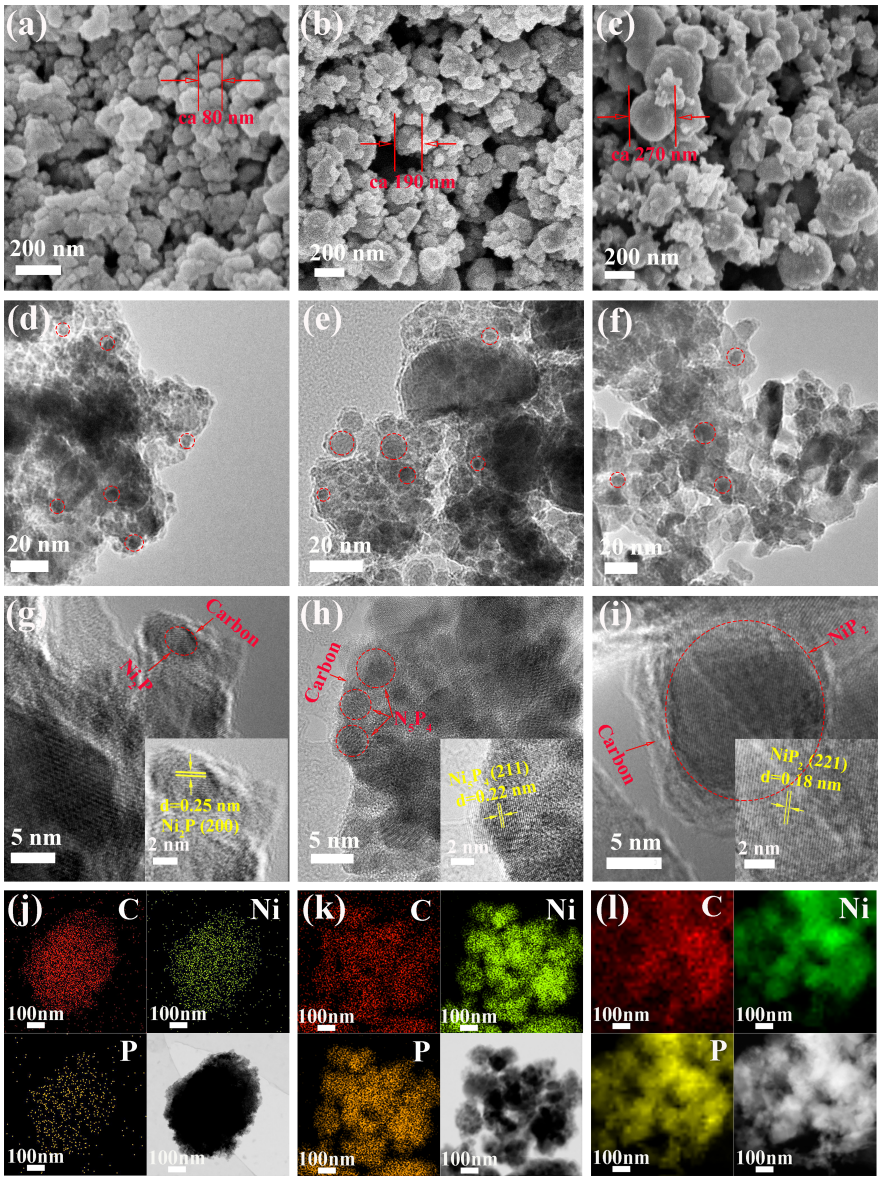

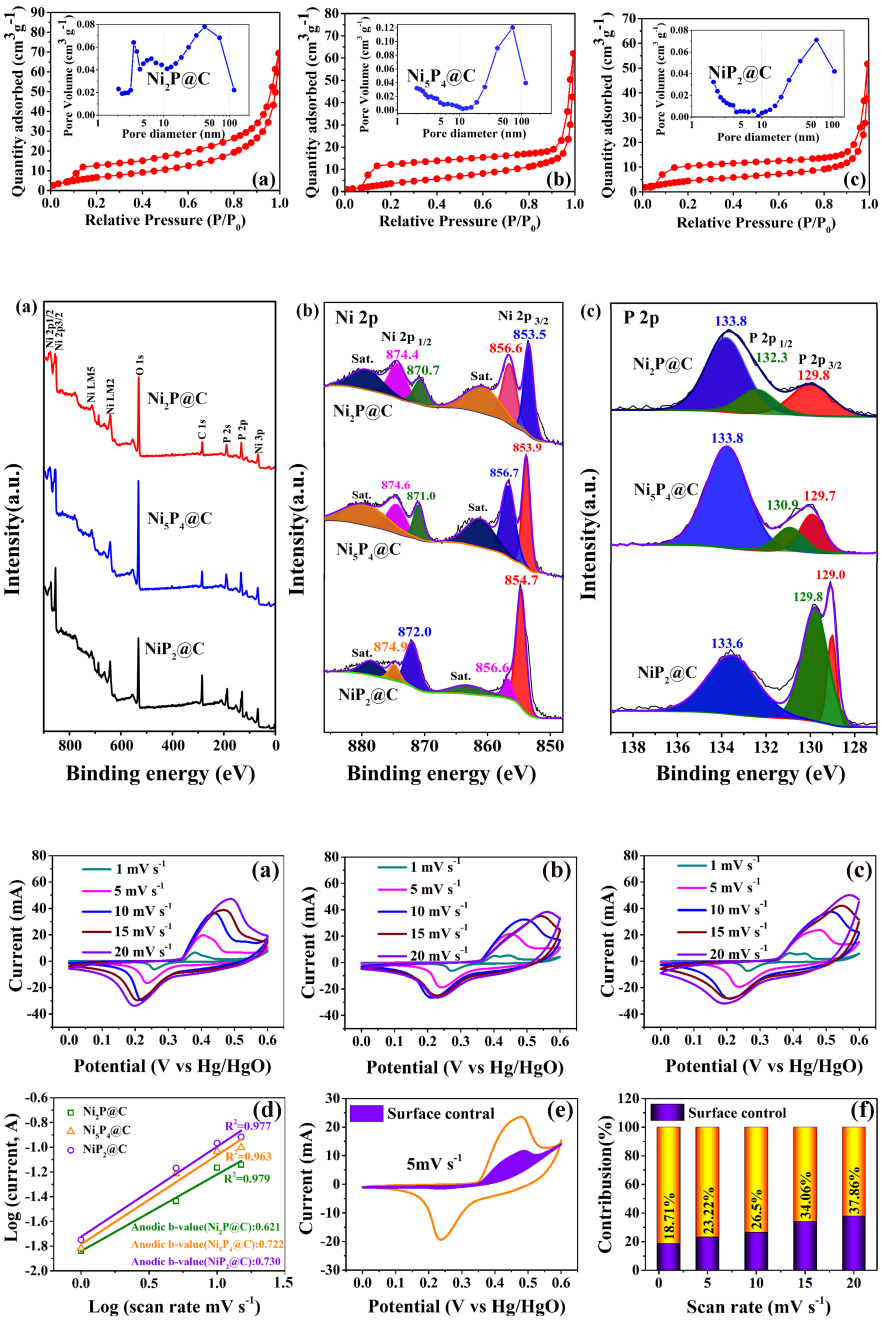

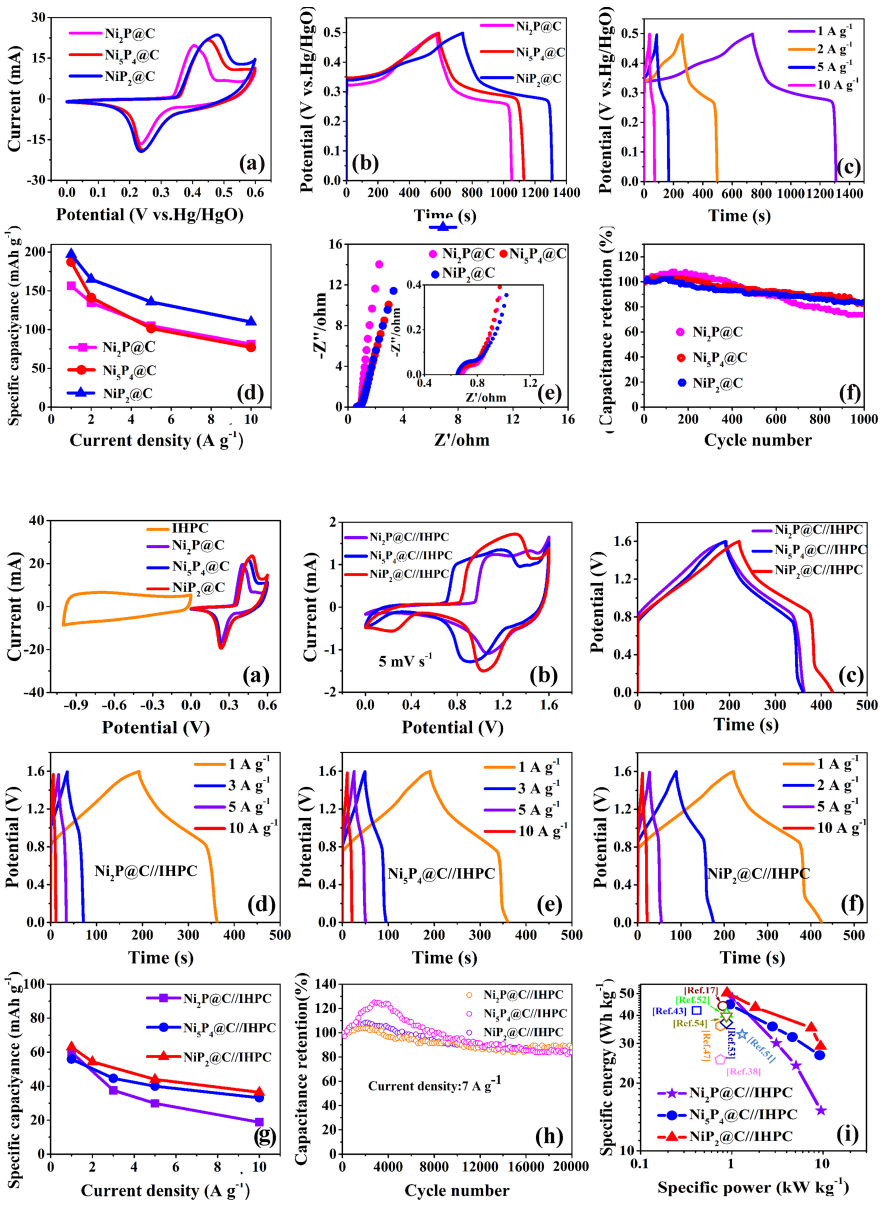

Hosted file

Table 1 .docx available at https://authorea.com/users/482811/articles/569239-one-step-solid-state-synthesis-of-nixpy-c-nanocomposites-for-high-performance-hybrid-supercapacitor